2015 © The Japan Society for Analytical Chemistry

Original Papers

Multimodal Imaging of Living Cells with Multiplex Coherent Anti-stokes Raman Scattering (CARS), Third-order Sum Frequency Generation (TSFG) and Two-photon Excitation Fluorescence (TPEF) Using a Nanosecond White-light Laser Source

Hiroki SEGAWA,*1 Masanari OKUNO,*2 Philippe LEPROUX,*3 Vincent COUDERC,*3 Takeaki OZAWA,*1 and Hideaki KANO*4,*5†

*1 *Department of Chemistry, School of Science, The University of Tokyo, 7-3-1 Hongo, Bunkyo, Tokyo 113–0033, Japan*
*2 *Department of Chemistry, Graduate School of Pure and Applied Sciences, University of Tsukuba, 1-1-1 Tennodai, Tsukuba, Ibaraki 305–8571, Japan*
*3 *Xlim Research Institute, CNRS-University of Limoges, 123 avenue Albert Thomas, 87060 Limoges cedex, France*
*4 *Institute of Applied Physics, University of Tsukuba, 1-1-1 Tennodai, Tsukuba, Ibaraki 305–8573, Japan*
*5 *Graduate School of Pure and Applied Sciences, University of Tsukuba, 1-1-1 Tennodai, Tsukuba, Ibaraki 305–8573, Japan*

The subnanosecond "white-light laser" source has been applied to multimodal, multiphoton, and multiplex spectroscopic imaging (M^3 spectroscopic imaging) with coherent anti-Stokes Raman scattering (CARS), third-order sum frequency generation (TSFG), and two-photon excitation fluorescence (TPEF). As the proof-of-principle experiment, we performed simultaneous imaging of polystyrene beads with TSFG and TPEF. This technique is then applied to live cell imaging. Mouse L929 fibroblastic cells are clearly visualized by CARS, TSFG, and TPEF processes. M^3 spectroscopic imaging provides various and unique cellular information with different image contrast based on each multiphoton process.

Keywords CARS, two-photon excitation fluorescence, microscopy, multiphoton, spectroscopic imaging

(Received November 29, 2014; Accepted December 29, 2014; Published April 10, 2015)

Introduction

Supercontinuum (SC) light sources have attracted much attention due to their capability in improving imaging techniques. Thanks to the broadband spectral profile and high spatial coherence of SC, high axial resolution for optical coherence tomography (OCT)[1,2] and high fluorescence efficiency for confocal microscopy[3-5] are demonstrated. Furthermore, ultrabroad spectral profile ranging from ultraviolet (UV) to visible or near infrared (NIR) can significantly simplify electronic and/or vibrational resonance spectroscopic systems or multicolor flow cytometric apparatus.[6-9]

Among the reported SC light sources, the sub-nanosecond fiber-based system is one of the most appropriate solutions from the viewpoints of compactness, cost-effectiveness and user-friendliness. It is widely recognized as the compact and low-cost "white-light laser". Typical SC generation is performed by launching monochromatic laser pulses into a photonic crystal fiber (PCF). The SC spectrum is constructed all along the PCF through the combined contribution of various third-order nonlinear optical effects such as self-phase modulation (SPM), cross-phase modulation (XPM), parametric four-wave mixing (FWM), modulation instability (MI), stimulated Raman scattering (SRS), and soliton effects.[10] The SC generation is strongly dependent on the specific structure of the PCF. The size of silica core, the diameter of air holes and their arrangement in the cladding region enable us to control dispersion property of the light propagation through the PCF. In particular, small-core PCFs spatially confine the laser pulses over large propagation length, while tailoring the zero-dispersion wavelength of the PCF can temporally confine the pulses without spreading. Both spatial and temporal confinement of the laser pulses in the PCF core drives various nonlinear optical processes and promotes the wavelength conversion, resulting in the SC generation.

The first demonstration of visible continuum generation in a PCF was performed in 2000 by propagating 100-fs pulses from a Ti:sapphire laser oscillator near the zero-dispersion wavelength of the fiber.[11] Later, white-light SC generation in a PCF was reported using 60-ps[12] and 0.8-ns[13] pump laser sources

† To whom correspondence should be addressed.
E-mail: hkano@bk.tsukuba.ac.jp

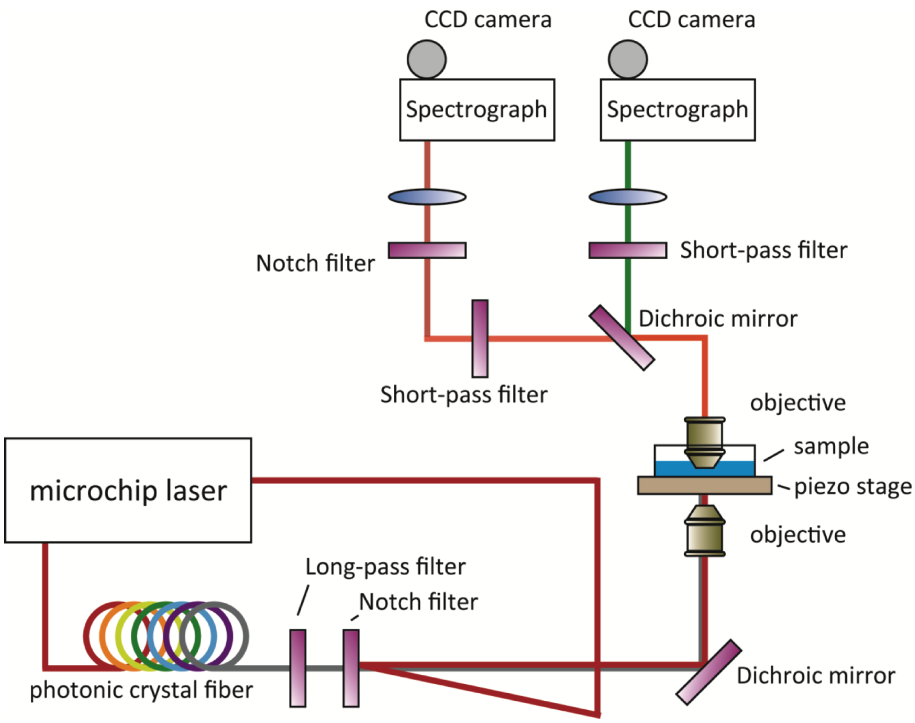

Fig. 1 Schematic of M^3 spectroscopic microscope (color version of figure is available online).

respectively. The latter experiment was the first demonstration of SC generation by using a passively Q-switched microchip laser. Continuous-wave (CW) visible SC generation was demonstrated much later, based on the trapping of dispersive waves by infrared solitons.[14,15]

The spectral profile of SC can also be tailored by the pumping scheme. Dual-wavelength pumping enables us to obtain homogeneous spectral broadening, smooth spectral profile, and single mode operation in the visible range.[16,17] By using the SC light source with dual-pumping scheme, we have reported the first demonstration of Raman optical activity (ROA) by coherent anti-Stokes Raman scattering (CARS) in the visible range.[18]

The SC has been widely used in microscopic imaging. Thanks to high photon density, we can perform multimodal, multiphoton, and multiplex spectroscopic imaging (M^3 spectroscopic imaging). So far, CARS, second harmonic generation (SHG), third harmonic generation (THG), and third-order sum frequency generation (TSFG) imaging have been reported by our group.[19,20] In the present study, we have extended our microscopic system further by launching another multiphoton channel, two-photon excitation fluorescence (TPEF).

TPEF microscopy is one of the most established techniques in multiphoton microscopy (MPM).[21] It has been widely used in life sciences to visualize intracellular molecules with intrinsic three-dimensional resolution. Recently, three-photon,[22] four-photon,[23] and even five-photon[24] excitation fluorescence microscopic techniques have been reported. Typical TPEF microscopy employs femtosecond mode-locked Ti:sapphire laser. Owing to NIR excitation, large penetration depth and low photodamage are expected. For fulfilling an electronic resonance condition, however, we need to tune the laser wavelength for each intracellular molecule. Since the two-photon allowed electronic state is different from the one-photon allowed state in general, the conventional absorption spectrum does not coincide with the two-photon absorption spectrum. In order to find the two-photon excitation resonance, the application of the SC light source is one of the simplest ways. Due to the ultrabroadband two-photon excitation, the electronic resonance condition should be automatically satisfied. A similar strategy has been employed in multiplex CARS microspectroscopy for fulfilling vibrational resonance conditions.[25,26] In the present study, we performed tri-modal (CARS, TSFG, and TPEF) multiplex spectroscopic imaging. First, we show the proof-of-principle experiment using polystyrene beads. Next, we applied this technique to living cells.

Experimental

Sample preparation

Polystyrene beads of 1-µm in diameter with and without orange fluorophore were purchased from Life Technologies and Polyscience, respectively. We made a mixture of these two types of beads, and sandwiched them with two cover slips. Mouse L929 fibroblastic cells were cultured on 3.5 cm glass-base dishes. The medium was D-MEM (Gibco) with 10% FBS (Gibco). Before the measurement, the culture was washed by phosphate buffered saline (PBS) and the medium was replaced by 2 – 3 mL PBS. In order to observe the TPEF signal from living cells, we used MitoTracker Orange CMTMRos (MTO; Life Technologies). The final concentration of MTO was about 200 nM. We followed the staining protocol published by the manufacturer.

Apparatus

The M^3 spectroscopic imaging system was developed by our group and has been already reported elsewhere.[19,20] Figure 1 shows the simple schematic of the system. A Q-switched microchip Nd:YAG laser is used as a light source. The center wavelength, temporal duration, and repetition rate are 1064 nm, 800 ps, and 33 kHz, respectively. First, a 1064-nm radiation

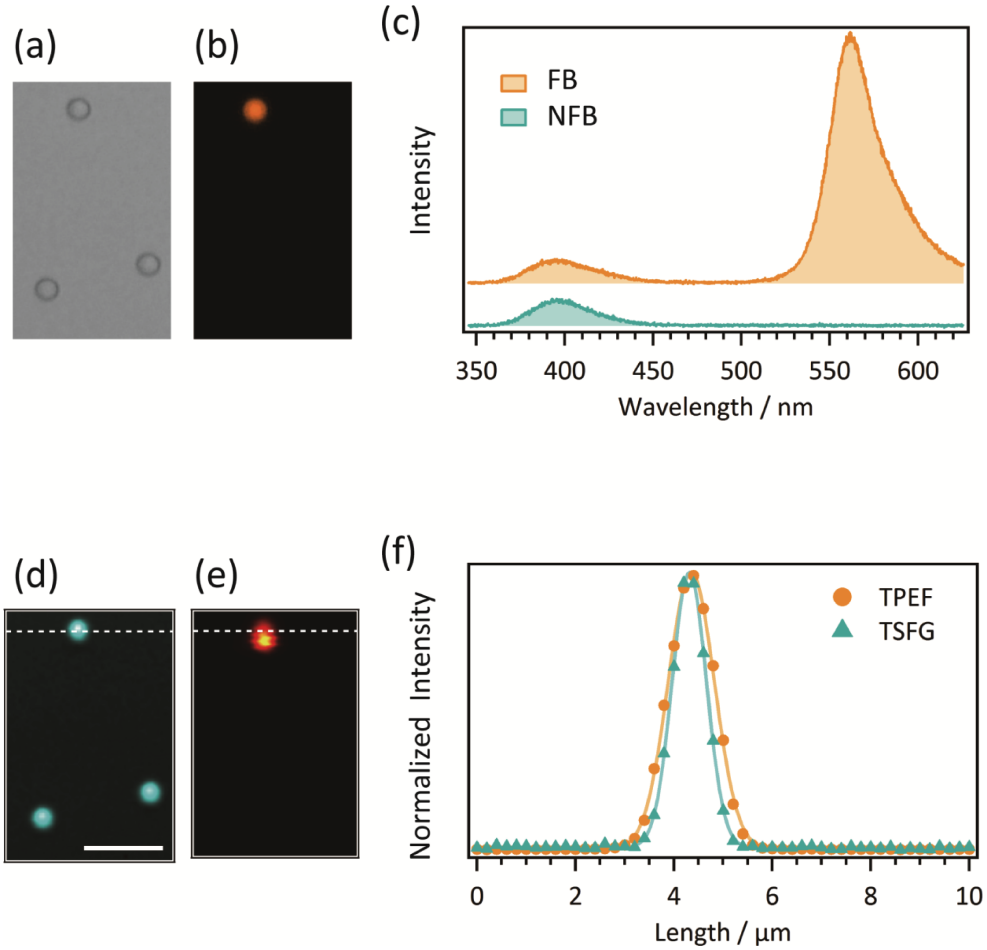

Fig. 2 Simultaneous imaging of FB and NFB with TSFG and TPEF. (a) Bright field image, and (b) one-photon fluorescence image of the sample. (c) Typical obtained spectra from FB and NFB. (d) TSFG, and (e) TPEF image. (f) Intensity plot along the white broken line in (d) and (e). The white bar shown in (d) indicates 5 µm (color version of figure is available online).

(fundamental) is divided into two. One is used for ω_1 laser (namely, pump and probe laser). The other is introduced into a PCF. Ultrabroadband SC ranging from visible to NIR is used as ω_2 laser (Stokes laser). After removing spectral components shorter than 1064 nm from the SC using a long-pass filter, ω_1 and ω_2 radiations are superimposed by a notch filter, and then introduced into a modified inverted microscope (Nikon: ECLIPSE Ti). Incident radiations are tightly focused onto a sample by the first objective lens. The sample is placed upon a piezo electric stage (PZT, Mad City Lab: Nano-LP200) for raster scanning. The forward propagating signals of nonlinear optical processes are collected by the second objective lens. The signals are then divided into NIR and UV-visible components by a dichroic mirror. For the transmitted NIR spectral component, collinear propagating ω_1 and ω_2 radiations are blocked by a short-pass filter and a notch filter. The CARS signal is then introduced into a spectrograph (Princeton Instruments: LS785) and detected by a CCD camera (Princeton Instruments: PIXIS 100BR). On the other hand, the reflected visible component contains TSFG and TPEF signals. After passing through a short-pass filter, the signals are detected by a spectrograph (Princeton Instruments: SpectraPro 300i) and a CCD camera (Princeton Instrument: PIXIS 100BR eXcelon). Exposure time was 50 ms per pixel. Bright field image and one-photon fluorescent image of samples are captured by a microscope-attached digital camera. Light sources for each image are a halogen lamp and a mercury lamp, respectively. For data analysis, maximum entropy method (MEM) and singular value decomposition (SVD) analysis were applied in order to retrieve denoised multiplex CARS spectra.[27-29]

Results and Discussion

Proof of principle experiment

In order to confirm the feasibility of multimodal imaging with TPEF and other nonlinear optical processes, we chose fluorescent beads as a test sample. The results of the mixture of non-fluorescent polystyrene beads (NFB) and fluorescent beads (FB) are shown in Fig. 2. As it was clear from the comparison of the bright field image (Fig. 2(a)) with the one-photon (conventional) fluorescence image (Fig. 2(b)), the bead at the top side was an FB, and the other two beads at the bottom side were NFB. Typical spectral profiles in the visible region at the FB and NFB positions are shown in Fig. 2(c). Based on our previous study,[19] the broadband signal around 400 nm was assigned as TSFG. Concerning the spectrum at the FB position, the other broadband signal was observed at around 560 nm. Since the spectral profile and the peak position coincided with those provided by the bead manufacturer (Life Technologies),

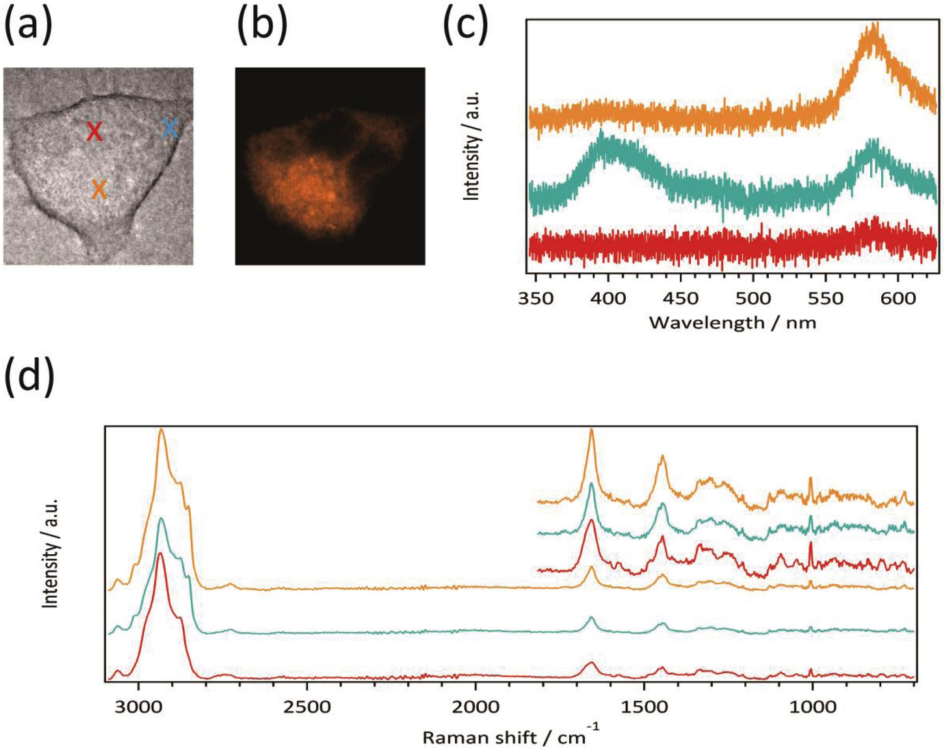

Fig. 3 An L929 fibroblast stained with MTO; bright field image (a), and one-photon (conventional) fluorescence image (b). Spectral profiles in visible (c), and NIR (d) regions. The insets in (d) are expanded spectra in the fingerprint region. The bottom axis of NIR spectra is converted into Raman shift. Colored crosses in (a) indicate the positions where corresponding spectra shown in (c) and (d) were obtained (color version of figure is available online).

we could safely assign that this broadband signal was TPEF from FB. The results of multimodal imaging using TSFG and TPEF are shown in Figs. 2(d) and 2(e). In the TSFG image (Fig. 2(d)), all three beads were visualized. On the other hand, we could recognize only one FB in the TPEF image (Fig. 2(e)) at the top side. The difference between Figs. 2(d) and 2(e) originated from the different contrast mechanism of each nonlinear optical process. TSFG is capable of label-free imaging, and takes place at an optically inhomogeneous area such as the interface of two layers with different refractive indices. The detailed signal generation mechanism has been already explained in our previous report.[30] In the present case, the refractive indices difference between the polystyrene beads and surrounding air provided the image contrast of TSFG. Since the bead diameter was 1 µm, it approximately corresponded to a point source for the multiphoton processes.

In contrast to TSFG, TPEF only visualized FB at the top. Since TPEF required fluorophore for signal generation, NFB was not visualized by TPEF. It is reasonable that the FB showed fluorescence through the two-photon excitation (TPE) with the 1064-nm radiation, because half of the excitation wavelength (1064 nm) corresponds to 532 nm, which is shorter than that of the fluorescence of FB in this study (around 560 nm). It should be noted that the TPEF image of FB did not show a round shape (see Figs. 2(d) and 2(e)). It was probably caused by the photobleaching effect of fluorescent dyes loaded on the bead. Since the raster scanning was performed from the bottom to the top, it is reasonable that the intensity of the TPEF signal from the bottom was larger than that from the top due to the photobleaching effect. Figure 2(f) shows the intensity profiles of TSFG and TPEF of FB along the white broken line in Figs. 2(d) and 2(e). It should be emphasized that the full-width at the half maximum (FWHM) of the signal intensity at the FB were different between TSFG and TPEF. The FWHMs were 0.82 and 1.1 µm for TSFG and TPEF, respectively. In other words, the spatial resolution of TSFG was better than that of TPEF. The difference of the FWHM can be explained mainly by the difference of the order of nonlinearity and by the different signal generation mechanisms. It is well known that a higher-order nonlinear process provides higher spatial resolution both in the axial and the lateral directions. In the present study, TPEF is the second order and TSFG is the third order nonlinear optical process. It is thus reasonable that the spatial resolution of TSFG was better than that of TPEF as shown in Fig. 2(f).

Imaging of mammalian cells

Next we measured L929 cells stained by MTO (see Figs. 3(a) and 3(b)). Typical spectral profiles due to various nonlinear optical processes in both UV-visible and NIR regions are shown in Figs. 3(c) and 3(d). In the UV-visible spectrum (Fig. 3(c)), we can recognize two broad bands. One around 400 nm was assigned as TSFG, and the other around 580 nm was assigned as TPEF from MTO. The spectral profile of the TPEF signal was consistent with the fluorescence spectral data provided by the manufacturer. The three spectral profiles in Figs. 3(c) and 3(d) were obtained at the positions indicated by each colored cross in the bright field image (Fig. 3(a)). The TPEF signal reflected the fluorescence intensity of MTO at each point. In the NIR region, multiplex CARS signals were detected (Fig. 3(d)). In the present study, M^3 spectroscopic imaging with CARS, TSFG and TPEF was successfully demonstrated. To the best of our knowledge, this is the first report of simultaneous

spectroscopic detection of the multiplex CARS and TPEF using a nanosecond laser source. As mentioned in the experimental section, multiplex CARS spectra shown in Fig. 3(d) were obtained after data processing using MEM and SVD analysis. MEM is one of the phase retrieval techniques. Raw CARS spectra are severely distorted due to coherent interference between the vibrationally resonant and nonresonant terms. MEM retrieves Im[$\chi^{(3)}$] spectra, which correspond to the resonant term in CARS spectra. The information contained in Im[$\chi^{(3)}$] spectra is the same as that in spontaneous Raman spectra.[27,29] In other words, Im[$\chi^{(3)}$] spectra is linear to the number of molecules, and we can apply the well-established band assignment to Im[$\chi^{(3)}$] spectra. On the other hand, SVD analysis is used for noise reduction.[28] Spectra shown in Fig. 3(d) is Im[$\chi^{(3)}$] spectra after above mentioned data processing.

Im[$\chi^{(3)}$] spectra provide rich molecular structural information. A large band was observed around 2900 cm^{-1}. This band is composed of CH_3 stretch (2932 and 2871 cm^{-1}) and CH_2 stretch (2847 cm^{-1}) vibrational modes. Orange and blue spectra in Fig. 3(d) showed the CH_2 stretch band larger than that in the red. It is noticeable that TPEF of MTO was also detected in the orange and blue spectra. Since the band intensity of the CH_2 stretch vibrational mode corresponds to the amount of lipid molecules,[31,32] this result indicates mitochondria, or adjacent mitochondria, contain relatively higher quantity of lipids. In the fingerprint region (800 – 1800 cm^{-1}), many Raman bands corresponding to molecular skeletal vibrations were observed. For example, the band around 1650 cm^{-1} was assigned as the superposition of *cis* C=C stretch and amide I mode bands of proteins. Although the peak position of this band in three spectra in Fig. 3 was similar to each other, the shape and the sharpness of the band were slightly different. Namely, orange and blue spectra gave sharper bands than that in the red. The sharp C=C stretch band is characteristic of unsaturated lipid molecules. Thus the difference of the band shape is consistent with the assignment of the CH stretch bands. There was another large band around 1450 cm^{-1}. This band was assigned as the CH bend mode, which was decomposed mainly into CH_3 degenerate deformation (1456 cm^{-1}) and CH_2 scissors (1440 cm^{-1}) modes. In the fingerprint region, we could recognize the position-specific small bands. For example, a weak shoulder band was observed around 1480 cm^{-1} in particular in the red spectrum. This band was assigned as the purine ring stretch mode.[32,33] This band can be used as the marker band of nucleic acid because adenine or guanine, kind of nucleic acid bases, contain purine ring. Purine ring also gives a band at 1580 cm^{-1}, and this was also detected in the red spectrum. Thus the position at the red cross corresponded to the inside of the nucleus. It is reasonable that no or very weak TPEF signal was detected from the position at the red cross (see Figs. 3(a) – 3(c)), because no mitochondria exists inside the nucleus. Moreover, the red spectrum showed many other characteristic bands such as PO^{2-} stretch (1096 cm^{-1}), breathing mode of phenylalanine residue (1003 cm^{-1}).

Based on these assignments, multimodal images that correspond to the distribution of various molecular species can be constructed by calculating the intensity of the Raman band in Im[$\chi^{(3)}$] spectra through curve fitting. The multimodal images are shown in Fig. 4. Each image corresponds to (a) TSFG, (b) TPEF, (c) purine ring stretch (nucleic acid), (d) CH_3 degenerate deformation (protein and lipid), (e) CH_2 scissors (lipid), and (f) phenylalanine residue (protein), respectively. The cell shown in Fig. 4 is the same as that in Fig. 3. TPEF image (Fig. 4(b)) well coincided with the one-photon (conventional) fluorescence image in Fig. 3(b). Due to the low signal-to-noise ratio, contrast

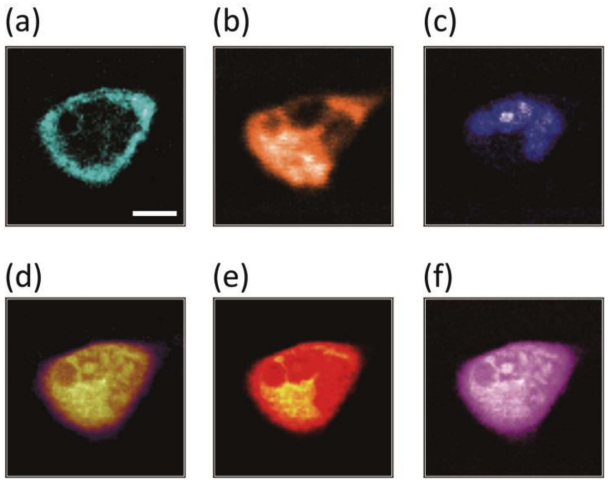

Fig. 4 M^3 spectroscopic imaging of an L929 cell. (a) TSFG, (b) TPEF, (c) purine ring stretch (1480 cm^{-1}), (d) CH_3 degenerate deformation (1456 cm^{-1}), (e) CH_2 scissors (1440 cm^{-1}), and (f) phenylalanine residue (1003 cm^{-1}). The white bar in (a) indicates 10 µm (color version of figure is available online).

of TPEF image was not as good as the one-photon fluorescence image. It should be emphasized, however, that the TPEF, CARS and TSFG were obtained from the same position simultaneously, because three nonlinear processes take place with the same excitation light source, namely the nanosecond laser source. This enables us to perform spatially correlated combinational spectral analysis of CARS, TSFG and TPEF signals. For example, CARS at the CH_2 scissors mode (Fig. 4(e)) gave high image contrast at cellular cytoplasm. It is worthwhile to note that the spatial pattern of CH_2 and TPEF images were similar to each other. In general, CARS or Raman images at CH_2 bend and stretch vibrational modes were widely used to detect lipid droplets inside the adipocytes.[34-36] In the case of fibroblasts, however, formation of lipid droplets depends on various conditions such as the composition of culture medium. In the present study, no droplet-like structure was observed in Fig. 4(e). Therefore, the coincidence of CARS at the CH_2 scissors mode and TPEF images means that membrane-rich mitochondria provided relatively large intensity at the CH_2 bend/stretch mode in the CARS signal.

In contrast to the other images, the TSFG image (Fig. 4(a)) showed a unique spatial pattern. That is to say, only the edge part of the cell was visualized. In order to investigate the reason for the unique contrast in the TSFG image, we measured the axial direction (XZ) images of another L929 cell. Figure 5 is the XZ direction images of (a) TSFG, (b) CARS at CH_2 stretch (2847 cm^{-1}), (c) CARS at purine ring (1580 cm^{-1}) and (d) CARS at phenylalanine residue (1003 cm^{-1}), respectively. TSFG image (Fig. 5(a)) clearly showed that the boundary of the cell and surrounding medium or glass was visualized. As mentioned in the proof-of-principle section, TSFG is sensitive to the optical heterogeneity such as the interface between two layers with different refractive indices. Therefore, TSFG visualized the interface between cell cytoplasm and medium, namely boundary of the cell. From the morphological point of view, the boundary of a cell corresponds to a plasma membrane. We could thus conclude that the XY image (Fig. 4(a)) visualized the cellular membrane. Plasma membrane-sensitive TSFG imaging enables spatially correlated membrane-selective CARS spectral analysis. In other words, our system can evaluate the molecular property

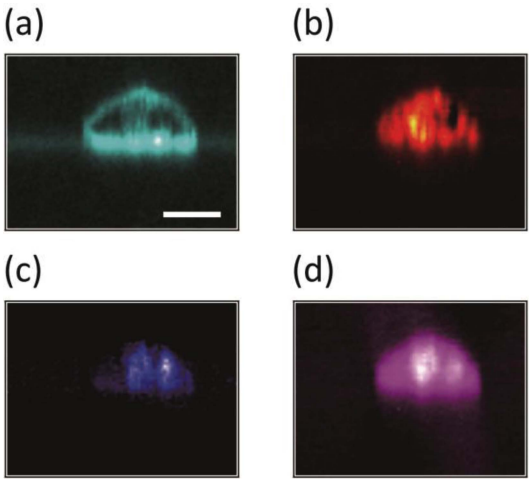

Fig. 5 M^3 spectroscopic imaging of an L929 cell in the XZ (axial) direction. (a) TSFG, (b) CH_2 stretch (2847 cm^{-1}), (c) purine ring (1580 cm^{-1}), and (d) phenylalanine residue (1003 cm^{-1}). The white bar in (a) indicates 10 µm (color version of figure is available online).

of a plasma membrane such as the composition of different lipid molecules through detailed Im[$\chi^{(3)}$] spectral analysis.

Conclusions

Exploring mulimodality of nonlinear optical imaging is of great importance because the combinational analysis of multiple nonlinear processes possibly provides more detailed molecular information on biological samples. In this study, we demonstrated that the subnanosecond white-light laser source was applicable to M^3 spectroscopic imaging with TSFG, CARS and TPEF. In the proof-of-principle experiment, we showed simultaneous imaging of polystyrene beads with TSFG and TPEF. The spatial resolution of TSFG was shown to be higher than that of TPEF mainly due to the difference of the order of nonlinearity. In the application to live cell imaging, we succeeded in M^3 spectroscopic imaging with TSFG, CARS and TPEF. Each image provided various molecular information due to the different contrast mechanisms. In particular, TPEF selectively visualized mitochondria inside a living L929 cell stained by MTO, and TSFG visualized a plasma membrane. It is notable that TPEF spectra of MTO and fluorescent beads showed different spectral profiles. This result indicates that spectral TPEF detection enables multicolor TPEF imaging using similar but spectroscopically different fluorophers based on spectral analysis. Since there is no need to tune the excitation wavelength, two-photon excitation using the SC light source is powerful in the spectroscopic imaging. Therefore, our M^3 spectroscopic imaging would open new frontiers in bio-analysis, and become a promising tool for medical imaging.

Acknowledgements

This work was supported by the JSPS bilateral joint research project (SAKURA program) and The NOVARTIS Foundation (Japan) for the Promotion of Science. The authors thank Prof. Hiro-o Hamaguchi for his guidance, support, discussion, and encouragement throughout the present study. The authors thank the LEUKOS company for technical support with the dual-output supercontinuum light source. The authors gratefully acknowledge J. Ukon, UKON CRAFT SCIENCE, Ltd. for assisting with a fruitful collaboration between Japanese and French labs.

References

1. B. Povazay, K. Bizheva, A. Unterhuber, B. Hermann, H. Sattmann, A. F. Fercher, W. Drexler, A. Apolonski, W. J. Wadsworth, J. C. Knight, P. St. J. Russell, M. Vetterlein, and E. Scherzer, *Opt. Lett.*, **2002**, *27*, 1800.
2. N. Nishizawa, Y. Chen, P. Hsiung, E. P. Ippen, and J. G. Fujimoto, *Opt. Lett.*, **2004**, *29*, 2846.
3. K. Lindfors, T. Kalkbrenner, P. Stoller, and V. Sandoghdar, *Phys. Rev. Lett.*, **2004**, *93*, 037401.
4. K. Shi, P. Li, S. Yin, and Z. Liu, *Opt. Express*, **2004**, *12*, 2096.
5. D. Wildanger, E. Rittweger, L. Kastrup, and S. W. Hell, *Opt. Express*, **2008**, *16*, 9614.
6. V. Kapoor, F. V. Subach, V. G. Kozlov, A. Grudinin, V. V. Verkhusha, and W. G. Telford, *Nat. Methods*, **2007**, *4*, 678.
7. W. G. Telford, F. V Subach, and V. V. Verkhusha, *Cytometry, Part A*, **2009**, *75*, 450.
8. C. H. Camp, S. Yegnanarayanan, A. A. Eftekhar, H. Sridhar, and A. Adibi, *Opt. Express*, **2009**, *17*, 22879.
9. A. Labruyère, A. Tonello, V. Couderc, G. Huss, and P. Leproux, *Opt. Fiber Technol.*, **2012**, *18*, 375.
10. J. M. Dudley and S. Coen, *Rev. Mod. Phys.*, **2006**, *78*, 1135.
11. J. K. Ranka, R. S. Windeler, and A. J. Stentz, *Opt. Lett.*, **2000**, *25*, 25.
12. S. Coen, A. H. L. Chau, R. Leonhardt, J. D. Harvey, J. C. Knight, W. J. Wadsworth, and P. S. J. Russell, *Opt. Lett.*, **2001**, *26*, 1356.
13. L. Provino, J. M. Dudley, H. Maillotte, N. Grossard, R. S. Windeler, and B. J. Eggleton, *Electron. Lett.*, **2001**, *37*, 558.
14. J. C. Travers, A. B. Rulkov, B. A. Cumberland, S. V. Popov, and J. R. Taylor, *Opt. Express*, **2008**, *16*, 14435.
15. A. Kudlinski, G. Bouwmans, O. Vanvincq, Y. Quiquempois, A. Le Rouge, L. Bigot, G. Mélin, and A. Mussot, *Opt. Lett.*, **2009**, *34*, 3631.
16. P. A. Champert, V. Couderc, P. Leproux, S. Février, V. Tombelaine, L. Labonté, P. Roy, C. Froehly, and P. Nérin, *Opt. Express*, **2004**, *12*, 4366.
17. V. Tombelaine, C. Lesvigne, P. Leproux, L. Grossard, V. Couderc, J. L. Auguste, J. M. Blondy, G. Huss, and P. H. Pioger, *Opt. Express*, **2005**, *13*, 7399.
18. K. Hiramatsu, H. Kano, and T. Nagata, in Abstracts of 24th International Conference on Raman Spectroscopy, ed. J. Popp and V. Deckert, **2014**, Jena, Germany, Thp-HS4-127.
19. H. Segawa, M. Okuno, H. Kano, P. Leproux, V. Couderc, and H. Hamaguchi, *Opt. Express*, **2012**, *20*, 9551.
20. H. Segawa, Y. Kaji, P. Leproux, V. Couderc, T. Ozawa, T. Oshika, and H. Kano, *J. Biophotonics*, in press, doi: 10.1002/jbio.201400059.
21. W. Denk, J. Strickler, and W. W. Webb, *Science*, **1990**, *248*, 73.
22. S. Maiti, J. B. Shear, R. M. Williams, W. R. Zipfel, and W. W. Webb, *Science*, **1997**, *275*, 530.
23. H. Matsuda, Y. Fujimoto, S. Ito, Y. Nagasawa, H. Miyasaka, T. Asahi, and H. Masuhara, *J. Phys. Chem. B*, **2006**, *110*, 1091.
24. Q. Zheng, H. Zhu, S.-C. Chen, C. Tang, E. Ma, and X. Chen, *Nat. Photonics*, **2013**, *7*, 234.

25. H. Kano and H. Hamaguchi, *Appl. Phys. Lett.*, **2005**, *86*, 121113.
26. T. W. Kee and M. T. Cicerone, *Opt. Lett.*, **2004**, *29*, 2701.
27. M. Okuno, H. Kano, P. Leproux, V. Couderc, J. P. R. Day, M. Bonn, and H. Hamaguchi, *Angew. Chem., Int. Ed.*, **2010**, *49*, 6773.
28. H. J. van Manen, Y. M. Kraan, D. Roos, and C. Otto, *J. Phys. Chem. B*, **2004**, *108*, 18762.
29. E. M. Vartiainen, H. A. Rinia, M. Müller, and M. Bonn, *Opt. Express*, **2006**, *14*, 3622.
30. H. Segawa, N. Fukutake, P. Leproux, V. Couderc, T. Ozawa, and H. Kano, *Opt. Express*, **2014**, *22*, 10416.
31. J. P. Pezacki, J. a Blake, D. C. Danielson, D. C. Kennedy, R. K. Lyn, and R. Singaravelu, *Nat. Chem. Biol.*, **2011**, *7*, 137.
32. Y. Ozeki, W. Umemura, Y. Otsuka, S. Satoh, H. Hashimoto, K. Sumimura, N. Nishizawa, K. Fukui, and K. Itoh, *Nat. Photonics*, **2012**, *6*, 845.
33. A. Toyama, N. Hanada, J. Ono, E. Yoshimitsu, and H. Takeuchi, *J. Raman Spectrosc.*, **1999**, *630*, 623.
34. B. Prescott, W. Steinmetz, and G. J. Thomas, *Biopolymers*, **1984**, *23*, 235.
35. B. G. Saar, C. W. Freudiger, J. Reichman, C. M. Stanley, G. R. Holtom, and X. S. Xie, *Science*, **2010**, *330*, 1368.
36. Y. Ozeki, Y. Kitagawa, K. Sumimura, N. Nishizawa, W. Umemura, S. Kajiyama, K. Fukui, and K. Itoh, *Opt. Express*, **2010**, *18*, 13708.
37. T. Hashimoto, H. Segawa, M. Okuno, H. Kano, H. Hamaguchi, T. Haraguchi, Y. Hiraoka, S. Hasui, T. Yamaguchi, F. Hirose, and T. Osumi, *J. Cell Sci.*, **2012**, *125*, 6127.